Journal of Wind Engineering & Industrial Aerodynamics 253 (2024) 105865

Contents lists available at ScienceDirect

Journal of Wind Engineering & Industrial Aerodynamics

journal homepage: www.elsevier.com/locate/jweia

Streamline curvature effects generated by tornado-like flows on the aerodynamics of a low-rise structure

Stefano Brusco *, Gregory A. Kopp

Boundary Layer Wind Tunnel Laboratory, Faculty of Engineering, University of Western Ontario, London, ON, Canada, N6A 5B9

ARTICLE INFO

Keywords:
Tornadoes
Non-synoptic winds
Building aerodynamics
Streamline curvature
Low-rise buildings

ABSTRACT

This paper examines the streamline curvature effects on the aerodynamic pressure patterns induced by tornado-like flows on a low-rise structure. The analysis derives from the detailed scrutiny of a wind tunnel test campaign carried out at the WindEEE Dome tornado simulator. The simulated tornado-like flows were characterized by a swirl ratio such that the cores were characterized by multiple vortices. The tornado-like vortex was slowly translated across the chamber of the simulator. Surface pressure measurements were acquired on both the building model surface and on a circular ground plate around it, and synchronized with velocity measurements gathered from four Cobra probes installed in the proximity of the corners of the structure. These Cobra probes allowed the definition of the tornadic streamlines. Multiple nominally identical repeats were carried out to gather a robust estimation of conditionally-averaged pressure and velocity measurements based on the position of the tornado-like vortex. When comparing different cases characterized by similar conditions of upstream wind direction, the mean aerodynamic pressure patterns were revealed to be sensitive to the streamline curvature. Moreover, these are distinct than those generated from straight-line ABL winds, consistently calibrated upon the measurements from the Cobra probes in the upstream proximity of the building.

1. Introduction

In the last several years, interest in the study of tornadic winds has risen rapidly within the Wind Engineering community. The impacts of tornadoes are known to be linked with significant economic losses, as well as with important interruptions to social and economic functions, which may deeply affect local communities (Zuo et al., 2021). United States and Canada are particularly sensitive to them (Sills et al., 2020), but Europe and Asia have also been subjected to the extreme winds induced by tornadoes (e.g., Groenemejer and Kühne, 2014; Yang et al., 2018). Their importance has been acknowledged by the recently released ASCE 7-22 (2022), which is the first consensus standard to include design loads for buildings in tornadoes. However, a robust procedure to design structures to tornadic winds is still far from being resolved since knowledge about tornado winds is relatively modest. This is associated with the limited size of the phenomenon and its unpredictable and violent nature (Stevenson et al., 2023), as well as with its complexity. Therefore, the steps that compose the Davenport Chain (Davenport, 1961), consolidated through systematic studies on straight-line atmospheric boundary layer (ABL) winds (hereinafter, referred to ABL winds), hardly seem to be adequate for tornadic winds. This has been testified by recent investigations, such as the one proposed by Gairola et al. (2023), who focused on the effects of the ground roughness on the mean wind flow of tornado-like flows, which indeed require different considerations compared to the traditional framework based on ABL winds. In fact, generation of turbulence and the relevant scales and intensities are still not known (Wang et al., 2017; Zuo et al., 2021); hence, their effects cannot be clarified (Kopp and Wu, 2020). In addition, the link between wind field and aerodynamic loading in tornadic flows is also a subject that is far from being understood and resolved. The swirl ratio (e.g., Wang et al., 2022; Zhang et al., 2023) is expected to play a role in the definition of the tornado wind field and the bluff-body aerodynamics, since different tornado structures may lead to different interactions between the vortical structures and the body. Moreover, the static pressure gradient, the vertical angle of attack, the vertical wind field, as well as the translational and rotational wind speeds, are all quantities that may alter the traditional concepts of building aerodynamics and the consequent wind loading (Kopp and Wu, 2020). In particular, the presence of radial and tangential components of the wind speeds leads to curved streamlines, which may play a role in

* Corresponding author.
E-mail addresses: sbrusco@uwo.ca (S. Brusco), gakopp@uwo.ca (G.A. Kopp).

https://doi.org/10.1016/j.jweia.2024.105865
Received 28 November 2023; Received in revised form 25 July 2024; Accepted 9 August 2024
Available online 22 August 2024

producing vorticity patterns that differ from those generated by ABL wind, as suggested by investigations carried out at the Iowa State University (ISU) simulator. Specifically, Yang et al. (2011) studied a high-rise building model in tornado-like winds by measuring the resultant aerodynamic forces through a high-sensitivity load cell, as well as by identifying the vortical structures around it through a digital Particle Image Velocimetry (PIV) system. The turbulent flow structures generated around the model and the resultant wind loads were found to be significantly different than those generated in ABL winds for the same wind angle orientation. A second study was published by Hu et al. (2011), investigating a one-story gable-roofed building. They found that the separation bubble on the leeward wall may be significantly compressed if the tornadic wind field is highly curved, relative to the ABL case. Summarizing, the studies of tornadoes and their effects on structures are research subjects on which wind engineering research groups are particularly active, spanning from numerical (e.g., Gairola and Bitsuamlak, 2019; Gairola et al., 2024) and experimental (e.g., Chen et al., 2023; Romanic et al., 2023) techniques to reproduce the phenomena observed in full-scale measurements (e.g., Lombardo, 2018; Lombardo et al., 2023; Miller et al., 2024). A review paper containing the most recent advancements on the subject has been recently published by Haan Jr. et al. (2024).

Of particular interest for the current manuscript, Kopp and Wu (2020) conducted experiments on a 1:50 scale model of the Texas Tech University (TTU) Wind Engineering Research Field Laboratory (WERFL) at the WindEEE simulator at the University of Western Ontario. Tornado-like flows that slowly translated along a path that was perpendicular to the long side of the building. The tornado core diameter was approximately 3 times larger than the largest plan dimension of the building. They utilized surface pressures acquired by taps distributed on the ground plane to define an analytical fit of the static pressure distribution, calibrated on the formulation by Baker and Sterling (2018). This enabled the separation of the static contribution to the pressure field from the aerodynamically-induced one on the building. Moreover, they defined the reference wind velocity based on local measurements acquired by four Cobra probes installed in the proximity of the building edges. The simultaneous measurements of pressures and velocities allowed them to propose a framework to compare the loads induced in tornadoes and ABL winds based on the flow direction and magnitude estimated from the Cobra probes, as well as to draw the tornadic streamlines. Hence, they could capture the variation of the flow curvature and improve the estimate of the overall mean uplift through the ABL winds-based approach by shifting the wind azimuth angles in the range of about 7° to 25°. However, such shifting does not seem to be effective in predicting the aerodynamic loading on the walls and this is likely to be associated with the flow curvature altering the nature of the flow separations and reattachment (Kopp and Wu, 2020).

The objective of this paper is to extend the methodology of Kopp and Wu (2020) by connecting the presence of local pressure patterns, distinct from those induced by ABL winds, to the effects of the streamline curvature. The data used by Kopp and Wu (2020) are employed. This database is enriched with the addition of a case with the long side of the TTU WERFL building oriented 45° with respect to the tornado path. This configuration will be labelled as Case B, while the original one will be Case A throughout the paper. After this introduction, Section 2 briefly describes the WindEEE Dome and the experimental campaigns. Section 3 illustrates the methodology that was employed to define the tornadic streamlines. Section 4 examines selected mean pressure pattern distributions associated with specific characteristics of the upstream wind direction, discussing the presence of local effects that are different than those induced by ABL winds and linking them to the effects induced by the streamline curvature. Two sets of pressure patterns are chosen and compared to each other in Section 5, in order to understand how different streamline fields may generate distinct flow patterns around the structure. Section 6 summarises the main outcomes and develops future perspectives.

2. Wind tunnel methodology

2.1. The tornadic wind field

The WindEEE Dome is a testing facility that is designed to reproduce ABL winds, downbursts and tornado-like vortices (Refan and Hangan, 2018). It has a hexagonal plan shape and is characterized by two test chambers. The inner one has a diameter of 25 m and a height of 4 m. The generation of tornadic-like flows is made possible by the presence of 6 fans at the top chamber, which provide the required updraft, and periphery vanes at a given angle, which provide the required swirl. A bell-mouth allows the updraft flow to enter the upper chamber before being re-directed to the test chamber through the outer chamber. General descriptions of the facility are provided by Refan and Hangan (2016, 2018). Moreover, the bell-mouth may be translated along one of the symmetry axes of the inner chamber allowing a continuous change of the position of the tornado-like vortices.

The experiments that are analyzed in this paper have been extensively described by Kopp and Wu (2020) and are briefly reported herein for completeness. The tornado-like flows are characterized by a nominal swirl ratio, $S = 0.76$, where $S = \frac{r_0 \Gamma_{max}}{2Qh}$, r_0 is the updraft radius, Γ_{max} is the maximum circulation in the flow, Q is the flow rate per unit axial length, and h is the inflow depth. Additional information concerning the flow field may be found in Refan and Hangan (2018). The tornado core radius, r_c, is about 400 mm near ground level, while the vortex structure is characterized by multiple sub-vortices (e.g., Davies-Jones, 1986; Zhang et al., 2023).

No roughness elements were installed on the floor of the WindEEE Dome, which was set as nominally smooth. The tornado-like flows were translated across the center of the inner chamber for about 4 m at a speed of 57 mm/s (Kopp and Wu, 2020) along the y-axis of the Cartesian coordinate system (Fig. 1a and b). The vertical axis coincides with the z-direction. The Cartesian system is completed by the x-axis, which is normal to the tornado path (Fig. 1a and b). The instantaneous position of the bell-mouth, y_{bm}, was acquired through a laser transducer mounted on its roof. This position is converted in the quantity y_{TC} (Fig. 1) through an ensemble average and shifting procedure that will be explained in Section 2.2. For further details about the coordinate system, the reader is referred to Kopp and Wu (2020).

2.2. Pressure field measurements on the building and in its proximity

The pressure field was captured by a total of 204 taps that were almost uniformly distributed on the building model (Fig. 2a). The building has plan dimensions of 183 mm × 275 mm, with an eave height, H, of 78 mm. 27 pressure taps were installed on each of the shorter lateral walls, while the longer ones have 30. The remaining 90 taps are located on the roof. The X- and Y-axes of the structure are indicated in Fig. 1, noting that capital letters indicate building coordinate while lowercase are lab-centered coordinates. The Z-axis is vertical and positive if directed upwards. As shown in Fig. 1, the four corners are labelled as A, B, C, and D. The model was placed on a plywood circular plate of radius 1118 mm. This is equipped with 173 pressure taps distributed in a radially-symmetric manner (Fig. 2b) to measure the static pressure field induced by the tornado-like flows. This is instrumental in separating the total pressure acquired by the building taps into static and aerodynamic components, as discussed earlier.

The pressure measurement system was the same for taps installed on the building and on the baseplate, consisting of 0.3 m long PVC tubes with 1.35 mm inner diameter, two restrictors and 0.33 m long PVC tubes with an internal diameter of 0.9 mm. As documented by Kopp et al. (2005), this system leads to a nearly unity response for frequencies up to 200 Hz. Therefore, the pressure time-histories acquired by the pressure transducers were not corrected, but they were directly used and analyzed. Each pressure measurement (generically denoted as p) is

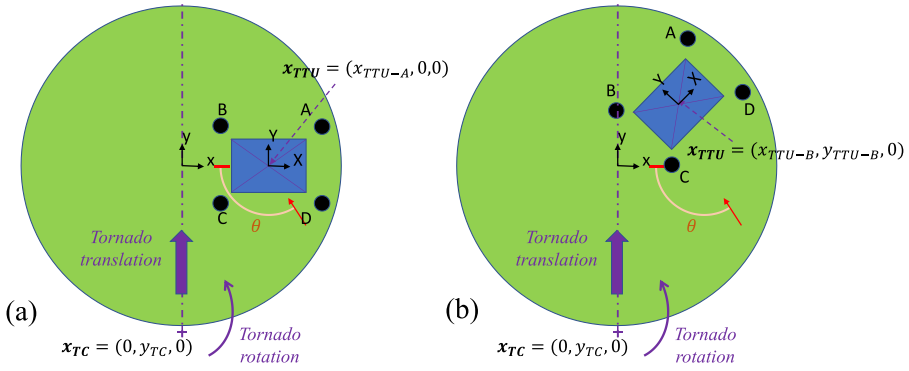

Fig. 1. Configurations tested at the WindEEE dome: (a) Case A; (b) Case B.

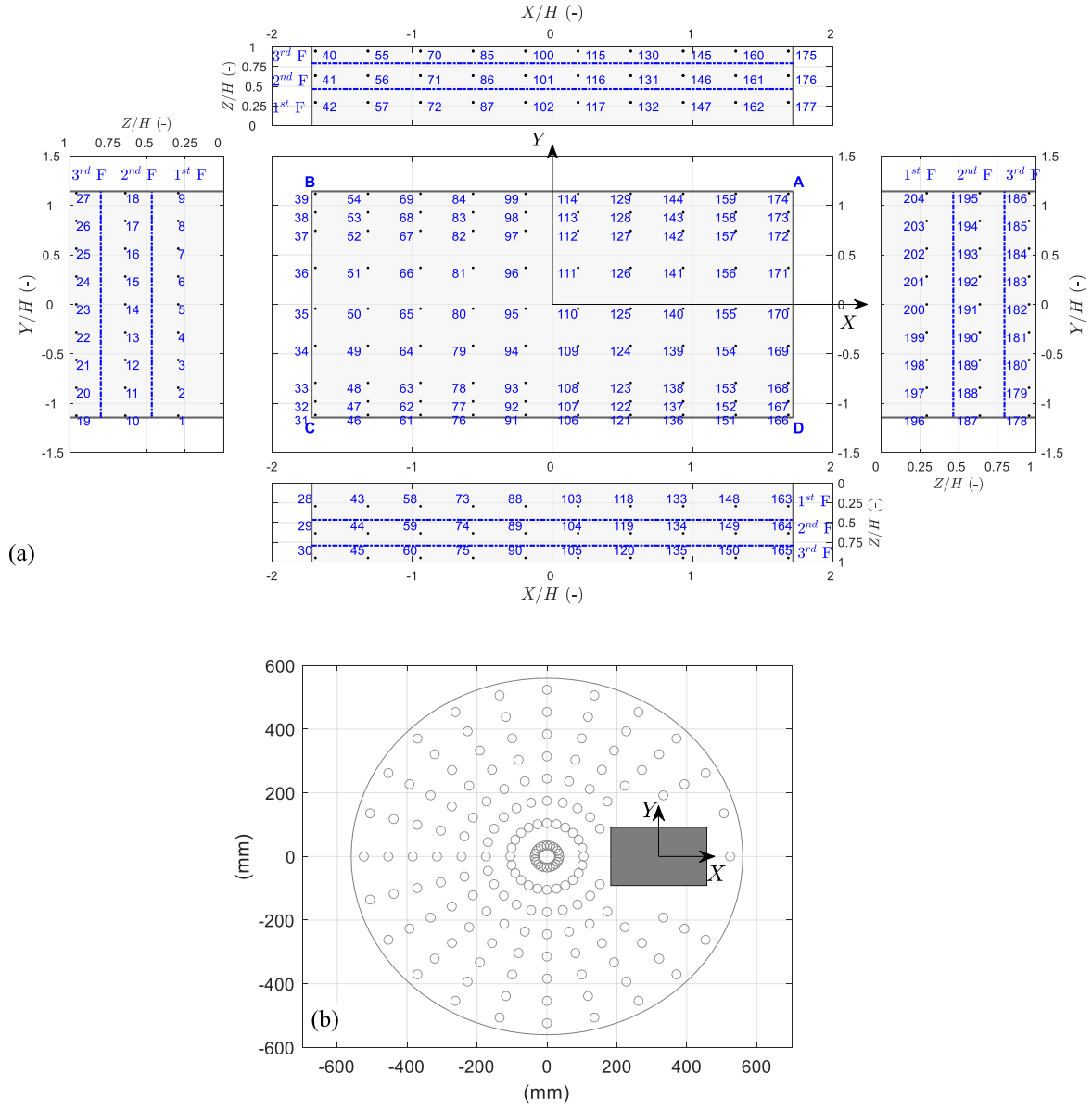

Fig. 2. Tapping scheme of the (a) 1:50 scale TTU WERFL building model and of the (b) baseplate.

referenced to the static pressure at the bell-mouth, p_{bm}. This latter one does not substantially vary with the position of the bell-mouth; hence, it constitutes a stable reference pressure for the measurements.

Two test configurations were considered. The first one featured the building with its *X*-axis perpendicular to the bell-mouth translation (Case A, Fig. 1a), while the second one concerned the model inclined 45° (Case B, Fig. 1b).

2.3. Wind field measurements in proximity of the building

Four Cobra probes were installed in proximity of each building corner, labelled as A, B, C, D (as the corresponding corners). These Cobra probes, called CP_A, CP_B, CP_C, and CP_D, were installed 72 mm (0.92 *H*) 45° from each building corner. The probe head was located above the roof of the building, 98 mm ($z_c = 1.26\ H$) above the ground. This does not constitute a typical choice for wind tunnel tests, since the measurements are likely to be affected by the presence of the building. On top of that, wake effects from the probes may propagate to the wall pressures. On the other hand, this solution is crucial for capturing the variation of the local flow curvature in the horizontal plane around the building. In fact, by fitting the velocity measurements with the theoretical formulation of Baker and Sterling (2018) for the radial and the tangential velocity components, it is possible to reconstruct the wind field induced by the tornado-like flows (Kopp and Wu, 2020). The translation of the tornado-like flows made the relevant generated wind field non-stationary; hence, the generated wind directions could not be captured by a fixed set of Cobra probes, which have a cone of acceptance of about 80 ° (± 40°). The Cobra probes were tentatively oriented such that they could measure the incoming wind when they were (approximately) windward of the building. To overcome the measurement limitations of the Cobra probes (i.e., the wind velocity is too low in magnitude, or it is directed outside of the cone of acceptance, see Fig. 2 in Kopp and Wu, 2020, for further details), three different combinations of probe orientations were applied, with 30 repeats of each. This is explained for Case A by Kopp and Wu (2020); analogously, a similar strategy has been adopted for Case B (i.e., Cases B – I, B – II, and B – III). Specifically, CP_A and CP_D were oriented to capture the wind for the tornado approaching the building ($y_{TC} < 0$ mm, Fig. 1a and b), while CP_B and CP_C were oriented to capture the wind once the tornado was leaving it ($y_{TC} > 0$ mm). Table 1 includes the information about the probe orientation defined for Case B, as well as the relevant number of nominally identical repeats that were carried out.

The Cobra probes are able to measure the incoming wind velocity in three components, viz., the longitudinal, lateral, and vertical. From these, it is possible to estimate the three components, *u*, *v*, and *w* parallel to the X, Y, and Z-coordinates (Section 2.1). Moreover, the velocity magnitude, $|\boldsymbol{u}|$, may be evaluated as:

$$|\boldsymbol{u}| = \sqrt{u^2 + v^2 + w^2}. \tag{1}$$

From the measurements, it is also possible to estimate the wind azimuth and elevation angles, θ and β, as:

$$\theta = \tan^{-1}\left(\frac{v}{u}\right); \tag{2}$$

Table 1
Description of the three combinations of probe orientations and relevant number of repeats for Case B.

Case B	Cobra probe A (CP_A), θ	Cobra probe B (CP_B), θ	Cobra probe C (CP_C), θ	Cobra probe D (CP_D), θ	Number of repeats
B - I	−65°	−195°	−180°	−95°	30
B – II	−95°	−180°	−180° °	−95° °	30
B - III	−65°	−195°	Not installed	Not installed	30

$$\beta = \tan^{-1}\left(\frac{w}{\sqrt{u^2 + v^2}}\right). \tag{3}$$

3. Methodology to define tornadic streamlines induced by tornado-like flows

Conditional-averaging procedures were defined based on y_{TC}. In particular, segments 10 mm long were defined and the acquired time histories of velocity and pressure were assigned to these according to the temporal variation of y_{TC}. The overall conditionally-averaged time histories for each of these quantities were obtained by stitching the different samples coming from each repeat. From this time-history, it was possible to estimate the ensemble mean and the ensemble root-mean-square fields. As in Kopp and Wu (2020), these will be simply referred to as the mean and rms values hereinafter, without the adjective 'ensemble' being used. They will be mathematically labelled with the symbols $\langle\cdot\rangle$ and rms $(\cdot)$, respectively.

Fig. 3 depicts the mean wind velocity vector profiles measured from the four Cobra probes for Case B. As for Case A, the variation of the estimated azimuth angle is significant for CP_D, ranging from approximately 120 ° to 45 ° over a 1.2 m translation of the tornado vortex, while CP_A is characterized by a more limited azimuthal variation, like for Case A. Oppositely, the measurements from the CP_B and CP_C, oriented to be able to measure the rear side of the tornado, indicate almost coincident wind velocities on the horizontal plan in magnitudes.

These measurements may be conveniently converted from a Cartesian coordinate system ($\boldsymbol{u} = (u,v,w)$) to a cylindrical one ($\boldsymbol{u} = (u_r, u_\alpha, w)$) attached to the tornado center, as done for Case A in Kopp and Wu (2020). In doing so, besides the azimuth angle, θ, it is necessary to define the distance from the tornado core $\Delta r = \sqrt{x^2 + (y - y_{TC})^2}$. As for Case A, the measurements from CP_B and CP_C (set to measure the rear side of the tornado) show a higher inflow (or radial) component u_r (for $1.5 < \Delta r/r_c < 3$), while CP_A and CP_B acquire higher tangential velocities u_α. This fact is likely to be related to the different effects generated by the translation of the tornado-like vortices on the different Cobra probes (Kopp and Wu, 2020). The information retrieved by these plots go even beyond the experimental outcomes, as demonstrated by Kopp and Wu (2020), who fit the data from Case A with the radially-symmetric analytical functions $u_r(r)$ and $u_\alpha(r)$ proposed by Baker and Sterling (2018). In particular, the measurements from CP_A and CP_B appeared to be less affected by the building if compared with CP_C and CP_D, and, hence, were adopted for the fitting. This step was instrumental to draw streamline fields (Fig. 2 a–c from their paper). Taking advantage of the Kopp and Wu method, the next figures show how such empirical fitting seems to be functional also for the experimental data gathered from Case B (magenta dots); the figures also report through black dots the data from Case A. The case of CP_B (Fig. 4b) shows an excellent agreement; the measurements from CP_A (Fig. 4a) follow the fit in a satisfactory way, especially for $\Delta r/r_c > 1.5$, although the magnitude of the tangential components are generally higher than the analytical fits.

Based on these outcomes, the analytical fit of the measurements from CP_A and CP_B (based on Case A) are suitable tools to reconstruct the wind field for Case B, confirming that the interference between wind field and building is limited. Therefore, the tornadic streamlines will be drawn by employing this fitting method, allowing a discussion about their effects on the aerodynamics of the building. For instance, they will enable the estimation of the velocity vector in the proximity of the building, even when this is not experimentally available. The field is drawn by attributing different weights to the measurements from CP_A and CP_B. CP_A is employed to draw the tornadic wind field for the building located at the front side of the tornado, while CP_B is used to model the wind field when the building is at the rear side. A smooth transition is applied between the two of them. The streamlines on the domain are drawn in Fig. 5, which also encloses specific velocity vectors experimentally evaluated

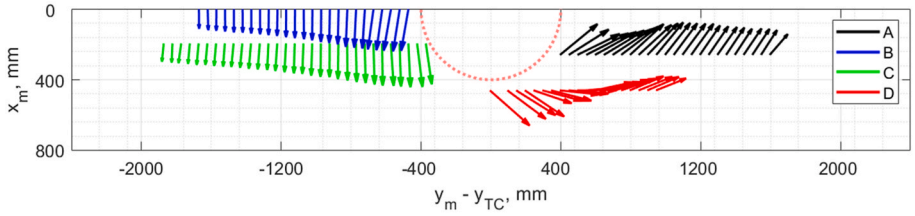

Fig. 3. Mean velocity vector $\boldsymbol{u}$ profiles for locations with respect to the tornado core estimated by the four Cobra probes measured every 100 mm for Case B. The red semi-circle denotes half of the tornado core.

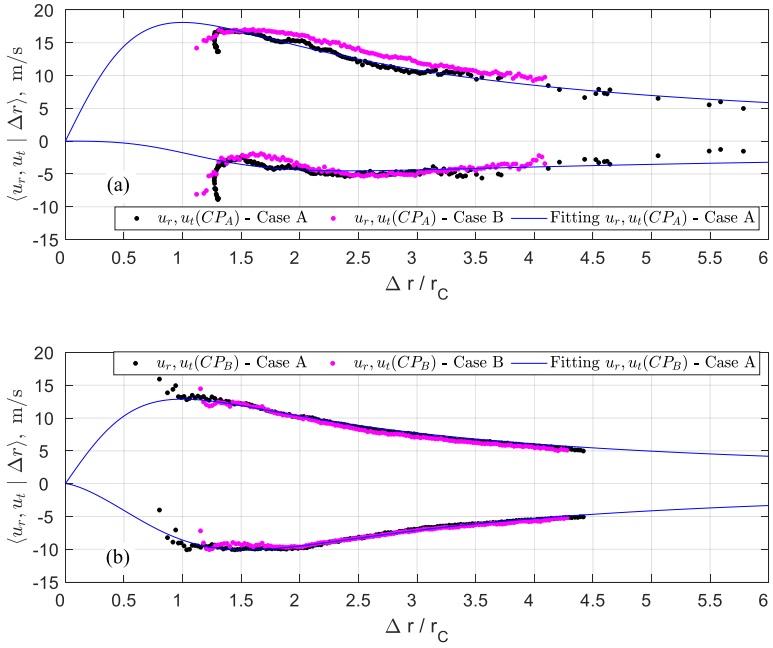

Fig. 4. Mean velocity components in cylindrical coordinate (radial and tangential) attached to the center of the translating tornado and relevant fitting based on Case A: (a) CP_A and (b) CP_B.

from CP_A (black) and CP_B (blue).

For the vertical component of the velocity, w, its estimation is reported in Fig. 6 versus the abscissa, $\Delta r/r_c$. The updraft in proximity of the tornado core may become rather sustained; therefore it may have an impact on the aerodynamics of the building. However, it is challenging to estimate the implications, since this aspect is deeply connected to tornado-like flows and is typically disregarded from traditional aerodynamic analyses of structures subjected to ABL winds.

Conditional-averaging procedures were carried out on the pressure measurements as well. The pressures measured from the taps on the radial ground-tap from Case A were fit with the theoretical formulation by Baker and Sterling (2018) (see Kopp and Wu, 2020 for a detailed description of the procedure). The same fitting function is used herein for Case B. This step is crucial to remove the static pressure associated with the tornado-like flows (p_s) from the total loading, and hence, to isolate the aerodynamic component of the loading, $p - p_s$.

4. Aerodynamic pressure patterns associated with tornado-like flows

In order to examine the effects played by the streamline curvature on the aerodynamics of the building model, this Section identifies specific aerodynamic pressure patterns from Case A and Case B. In particular, these are classified into three different categories. Section 4.1 groups cases characterized by the upstream wind direction perpendicular to the short side of the building. Section 4.2 concerns cases with the upstream wind direction oblique with respect to the building. Finally, Section 4.3 concerns different building orientations for the same distance between structure and the tornado core.

4.1. Upstream wind direction perpendicular to the short side of the building

The first case that is analyzed derives from Case A and is characterized by a vortex position at y_{TC} = -1125 mm (i.e., the building is located on the front approaching side of the tornado). It is called Case A – I. Fig. 7a shows the streamline field in the proximity of the building. The tornado core is indicated with a thicker red line. Fig. 7b shows the mean aerodynamic pressure field on the roof and on the circular ground plate, $\langle p - p_s|_{y_{TC}} \rangle$. The symbol $|_{y_{TC}}$ recalls that the measurements are linked with a specific position of the vortex. The baseplate and the building roof are framed into areas that are associated with single pressure taps. The (model-scale) magnitudes of the pressures are expressed (in Pascals) through the colorbar indicated on the top left of the graph. In addition, the mean wind velocity vectors corresponding to the four Cobra probes are indicated through arrows. These are in black if they are based on experimental data, when available. Their quantifications, in terms of magnitude, azimuth and elevation angle, are reported on the bottom left of Fig. 7b. On top of that, green arrows are drawn according to the analytical fitting. These ones, estimated for CP_B and CP_C, indicate a wind direction on the leeward side of the building that is approximately 15° misaligned with that on the windward face, being

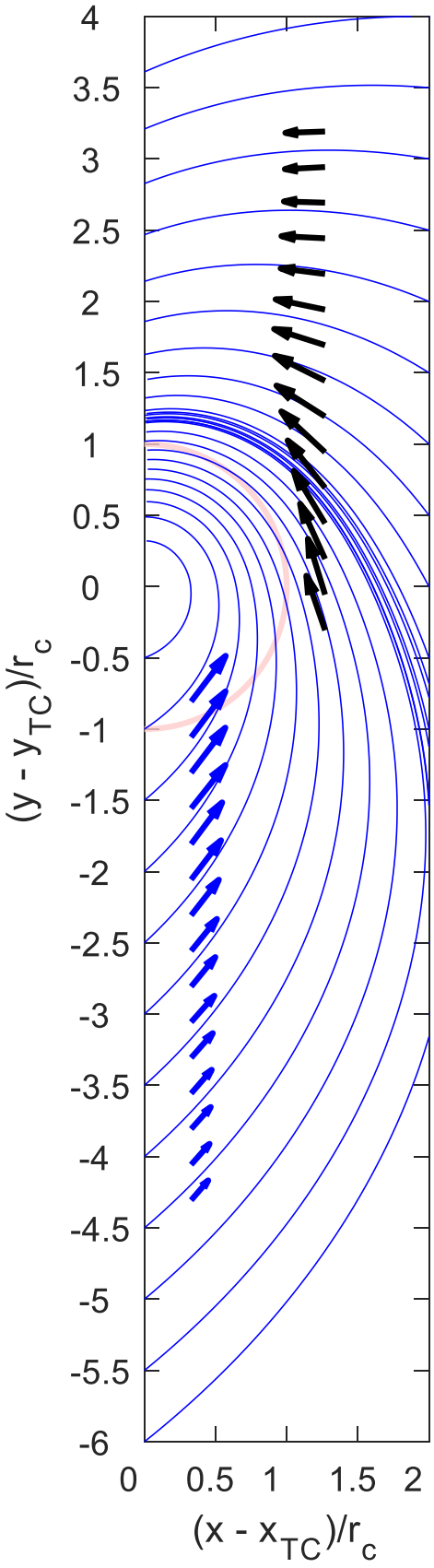

Fig. 5. Streamlines of planar mean velocities on the horizontal plan through a spatially-weighted average of CP_A and CP_B fits.

oriented towards "south-west".

The mean aerodynamic pressure patterns on the walls and the roof of the building are then provided in Fig. 8b, which also reports the same arrows associated with the mean wind velocity field on the corners of the unfolded building surfaces. Next to this plot, there are the mean aerodynamic pressure patterns that are estimated from tests conducted under straight-line ABL winds in Fig. 8a and c. These derive from a wind tunnel campaign conducted at the Boundary Layer Wind Tunnel 2 (BLWT2) at the University of Western Ontario on the same wind tunnel model for an open exposure. Further details about this set of experiments are found in Wu and Kopp (2016, 2018). The evaluated coefficients are then converted into pressures by using the dynamic pressure from the Cobra probes (details about the methodology for the comparison are provided by Kopp and Wu, 2020). For the case at hand, the measurements from CP_D are adopted (Fig. 8a), which are subsequently shifted 25° (Fig. 8c) as suggested by Kopp and Wu (2020), to consider the local variation of the flow curvature. Fig. 8a and c also include the mean velocity vectors from the four Cobra probes they are based on (in green), which for ABL winds are all equal.

The first comparison is made between the tornado measurements (Fig. 8b) and those from straight-line ABL winds based upon CP_D (Fig. 8a). The first glaring difference that may be noted concerns the absence of a symmetric pattern in the tornadic results, while Fig. 8a reflects an upstream ABL wind direction that is perpendicular to the short side of the building. In particular, clear distinctions are found on the pattern on the roof, which is known to be the dominant component for the aerodynamic behaviour of low-rise structures. In fact, Fig. 8b highlights the presence of conical vortices generated from the corner A that cannot be predicted in an ABL-based framework. Their presence generates a pattern of suction that propagates towards the side wall CD and the leeward wall BC, whose pressure distributions are again distinct from those shown in Fig. 8a. Shifting the orientation of CP_D (Fig. 8c) permits a better agreement of the patterns on the roof, as well as on the side wall CD (as discussed by Kopp and Wu, 2020), although the relevant aerodynamic loads become higher. Nonetheless, the localized suction on the leeward wall, BC, is again absent, and this appears to be an outcome typical of tornado-like flows, perhaps associated with the variation of the flow direction occurring along the long sides of the building.

An aerodynamically similar condition is now studied from Case B, labelled as Case B – I. In this case, $y_{TC} = 1105$ mm, hence the building is located on the rear side of the tornado. In analogy with Case A – I, the Cobra probes on the windward face, this time BC, experimentally indicate a flow direction that is perpendicular to that. From the analytical model of the flow direction, it is possible to infer a change of the wind orientation between the windward face, BC, and the leeward face, DA, in the order of 20–25°, as indicated by the magenta mean wind velocity vectors in correspondence of CP_A and CP_D. Fig. 9 is structured as Fig. 8, but Fig. 9c also encloses the pattern on the unfolded building surfaces, including the distributions on the walls.

The comments made for Case A – I appear to be applicable also in this circumstance. In fact, the pressure distribution reveals again a non-symmetric pattern, in spite of the fairly uniform flow direction registered on the windward face. Conical vortices are generated on the roof, this time starting from corner C. This is similar to Case A – I, where the conical vortices were again generated in the corner that was farther from the tornado core. The relevant suction pattern tends to propagate towards the side wall, AB, and the leeward wall, DA, whose distributions resemble those for the corresponding walls, CD and BC, from Case A – I. In effect, the prediction through an ABL-based framework (this time based on CP_C) leads to an underestimation of the loads on these walls, missing the relevant patterns, in particular for the leeward wall, DA.

Another case is presented herein, again extracted from Case B, called Case B – II, which is for $y_{TC} = 1755$ mm. This location again features the building on the rear side of the tornado, but with a greater distance than Case B – I. Therefore, the curvature of the streamlines is reduced (Fig. 10a), and the flow direction on the leeward side becomes more

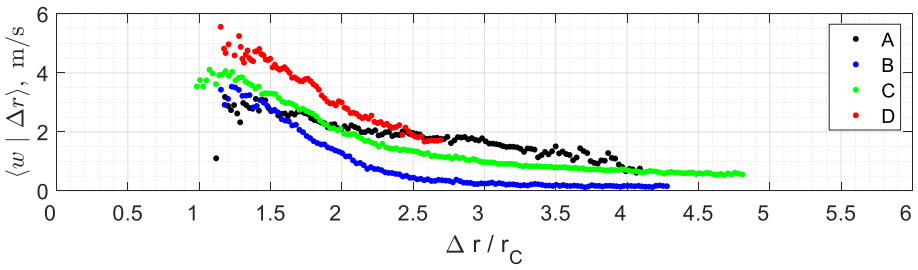

Fig. 6. Mean vertical velocity component (Case B). The measurement data are presented for accumulation times larger than 0.2 s.

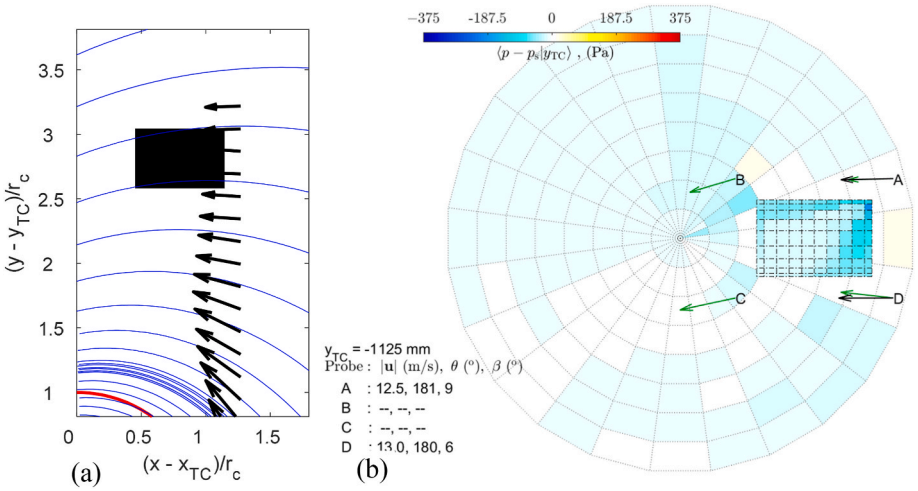

Fig. 7. (a) Tornadic streamlines and (b) mean pressure pattern on the roof and the baseplate for Case A – I.

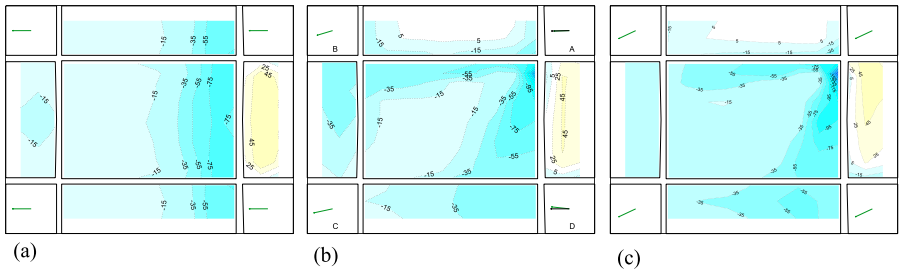

Fig. 8. Comparison between the mean pressure patterns estimated from tornado measurements (Case A – I) and straight-line ABL winds evaluated according to single probe measurements: (a) ABL winds based on CP_D, (b) tornado measurements, (c) ABL winds based on CP_D, $\langle\theta\rangle + 25°$.

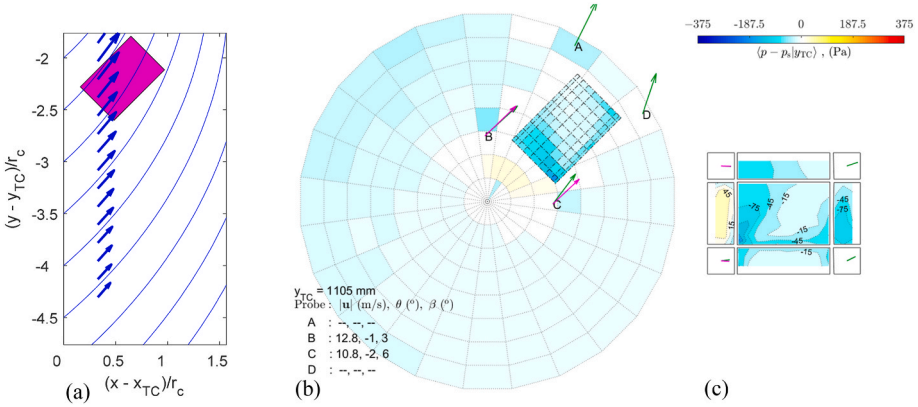

Fig. 9. (a) Tornadic streamlines, (b) mean pressure pattern on the roof and the baseplate, (c) mean pressure pattern on the unfolded building surface for Case B – I.

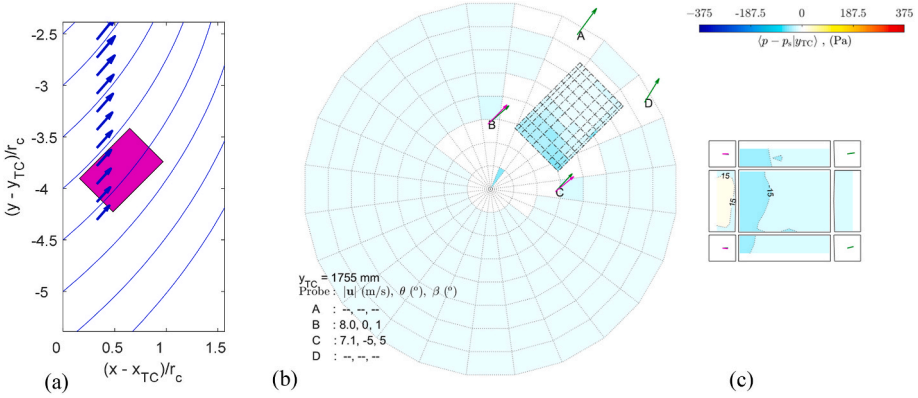

Fig. 10. (a) Tornadic streamlines, (b) mean pressure pattern on the roof and the baseplate, (c) mean pressure pattern on the unfolded building surface for Case B – II.

similar to that on the windward one. This seems to be reflected by the relevant mean aerodynamic pressure pattern (Fig. 10b and c). Indeed, the pattern on the roof becomes more symmetric, as those on the lateral walls. At the same time, the localized suction on the leeward wall vanishes.

In this Section, cases with upstream wind direction perpendicular to the short side of the building were examined. The role played by the streamline curvature appears to be reflected on the mean pressure distributions registered on the buildings, which are different from those observed in ABL winds for similar upstream wind direction. In fact, these distributions are characterized by cornering suctions, as well as by a localized increase of the load in the leeward walls (Cases A – I and B – I). Nonetheless, these effects are significantly mitigated once the streamline curvature is reduced (Case B – II).

4.2. Upstream wind direction oblique with respect to the building

The first three cases examined in this Section are all extracted from Case A, with the building on the rear side of the tornado, in particular for $y_{TC} = 375$ mm, 755 mm and 1755 mm (Case A – II, III, IV, respectively). This set is picked since, as noted by Kopp and Wu (2020) and in Section 3, the mean wind azimuths measured by CP_B and CP_C change little after the tornado passes the building. In analogy with Figs. 7 and 11 shows the tornadic streamlines for Case A – II and the mean aerodynamic pressure field on the geometry of interest. The azimuth angle registered from CP_C is 46°, which varies significantly (on the order of 30–35°) along the side, CD. Moreover, the streamline that passes through D tends to stay close to the building, bending and changing its orientation, as reflected by the inferred mean wind velocity vector of CP_A.

Following the structure of Fig. 8, Fig. 12 compares the mean aerodynamic pressure patterns from tornado-like flows with those from compatible ABL winds. These are based upon the measurements from CP_C (Fig. 12a), and by shifting them by 10° (Fig. 12c), as suggested by Kopp and Wu (2020) for this side of the tornado path.

The first comparison that is discussed concerns Fig. 12a and b. The patterns on the roof are characterized by the same origin as the conical vortices, i.e., corner C. However, the ABL-based case leads to an increase of the suction on the side BC, as well as on that side of the edge AB. On the other hand, the most evident discrepancy is found on the other side of the roof with a stronger suction found on the lateral edge DA in the tornadic case. It is worth noting that this occurs where there is the greatest difference in terms of flow field between straight-line ABL winds and tornado-like flows, as shown in Fig. 11a. The presence of different suction patterns between the two cases may reflect the presence of different vortical structures affecting the roof. Moreover, this seems to affect the leeward wall AB as well, which exhibits a strong localized suction that is missing in Fig. 12a. In fact, the pattern of the leeward wall appears distinct from the one typical of a straight-line ABL wind, which shows a continuous pressure recovery. As a final note, the presence of a stronger flow separation in the tornadic case is newly found on the lateral wall, DA, and this may be driven by the local flow field in correspondence of the corner D. In overall terms, the tornado case leads to a stronger aerodynamic loading on the wall DA and on the roof, while a reduction is found for the wall AB. The shifting of the wind direction of CP_C (Fig. 12c) is beneficial in reducing all these discrepancies; however, the generated pressure patterns are still distinct from

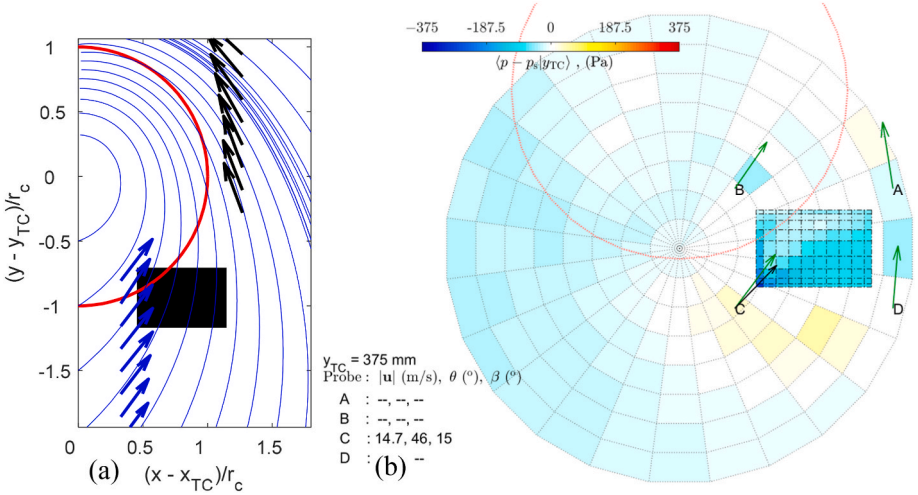

Fig. 11. (a) Tornadic streamlines and (b) mean pressure pattern on the roof and the baseplate for Case A – II.

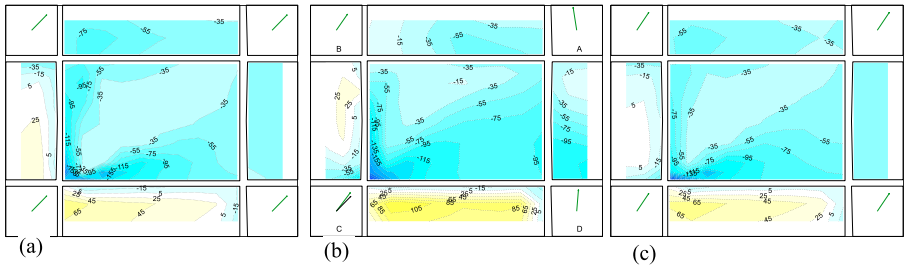

Fig. 12. Comparison between the mean pressure patterns estimated from tornado measurements (Case A – II) and straight-line ABL winds evaluated according to single probe measurements: (a) ABL winds based on CP_C, (b) tornado measurements, (c) ABL winds based on CP_C, $\langle\theta\rangle + 10°$.

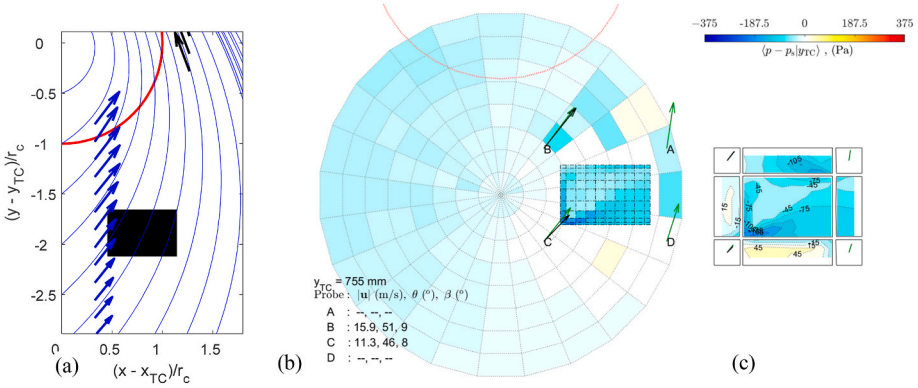

Fig. 13. (a) Tornadic streamlines, (b) mean pressure pattern on the roof and the baseplate, (c) mean pressure pattern on the unfolded building surface for Case A – III.

those induced by tornado-like flows.

Attention now is given to the variation of the pattern from tornado-like flows with the position of the vortex. Case A – III ($y_{TC} = 755$ mm) is shown in Fig. 13. As can be seen from the streamlines, and quantified in Fig. 13b, the azimuth estimated from CP_C is again 46°, the same as Case A – II. For this position, CP_B also provides data, and these indicate an azimuth equal to 51° and a mean wind velocity magnitude that is 40 % higher than the one from CP_C. The streamline curvature (Fig. 13a) is reduced, although it still reflects the rotational nature of the wind field.

From the pressure distribution on the unfolded building in Fig. 13c, it is again possible to note that the suction on the roof significantly propagates from corner C to the side DA of the roof. Moreover, a strong localized suction is newly found on the leeward wall AB, perhaps related to the pattern on the roof. This seems also to be highlighted by an increased suction experienced by the taps on the ground in front of this wall. If compared with Case A – II, this region seems to migrate towards the corner A, following the reduction of the streamline curvature. If compared with the results obtained from straight-line ABL winds, the tornadic case leads to higher aerodynamic loading for the walls DA and AB, as well as for the roof.

The last case that is examined from this set is Case A – IV ($y_{TC} = 1754$ mm, Fig. 14a and b). In this configuration, the aerodynamic loads are much reduced if compared with the other positions. The propagation of the suction on the roof seems to be more limited. As a matter of fact, the prediction through ABL-based approaches leads to comparable aerodynamic loading.

Now, two other cases are examined, both of them characterized by the presence of the building on the front side of the bell-mouth. The first one is extracted from Case A (Case A – V), and it is identified by $y_{TC} =$ -475 mm (Fig. 15).

The other case derives from Case B, and it is called Case B – III (Fig. 16). The bell-mouth is characterized by $y_{TC} =$ -715 mm; hence it is set back if compared with Case A – V (Fig. 15b and 16b). This choice is made to compare two situations that are more similar from an aerodynamic viewpoint, at least for the windward face, DA in both cases. Indeed, the pressure patterns observed in Fig. 15c and 16c denote

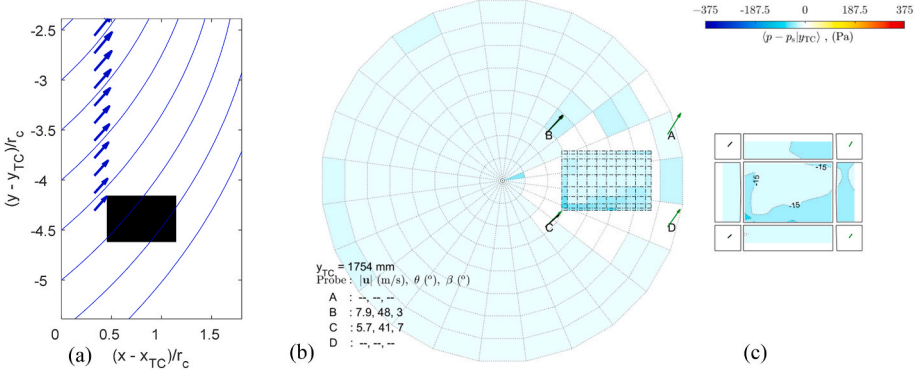

Fig. 14. (a) Tornadic streamlines, (b) mean pressure pattern on the roof and the baseplate, (c) mean pressure pattern on the unfolded building surface for Case A – IV.

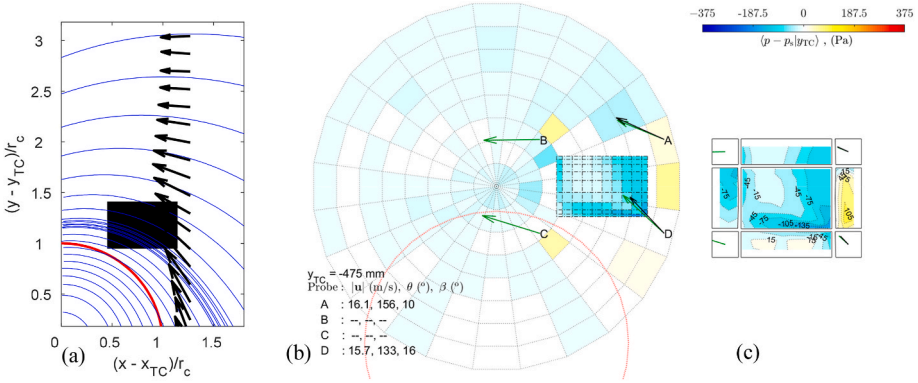

Fig. 15. (a) Tornadic streamlines, (b) mean pressure pattern on the roof and the baseplate, (c) mean pressure pattern on the unfolded building surface for Case A – V.

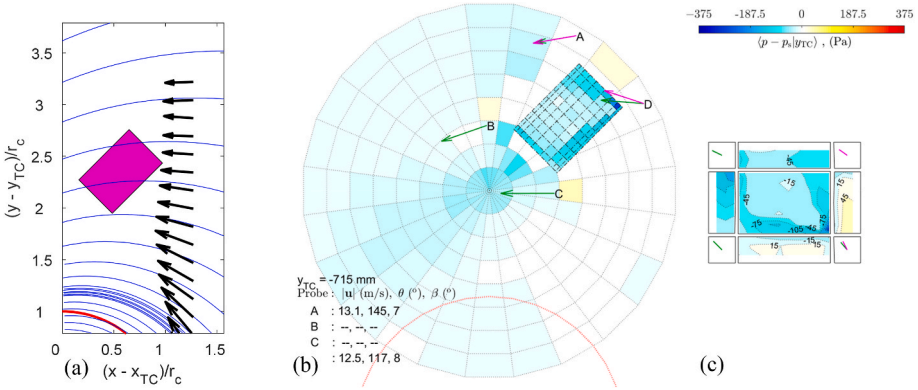

Fig. 16. (a) Tornadic streamlines, (b) mean pressure pattern on the roof and the baseplate, (c) mean pressure pattern on the unfolded building surface for Case B – III.

evident similarities. Firstly, in both cases the conical vortices start from corner D, and they tend to propagate towards the lateral and the leeward walls. Moreover, the walls AB reveal the presence of a localized suction towards the corner B, potentially linked with the pattern of the roof. Even more striking is the similarity between the walls BC, which both indicate the presence of local effects on the corner B. Particularly in Case B – III, such effect leads to strong discrepancies with the prediction through an ABL-based approach based on the measurements from CP_D.

In this Section, cases with a windward cornering wind direction were examined. As in Section 4.1, the role of the streamline fields in regions different than the upstream one is found to control the aerodynamics of the building (Cases A – II, A – III, A – IV). As a matter of fact, cases featured by different distances between the building and the tornado vortex but similar wind field in their proximity (Cases A – V, and B – III) are both characterized by analogous local effects, namely the conical vortices originated from the same corner and a localized suction on the leeward wall.

4.3. *Different building orientations at a fixed distance from the tornado centre*

The last case that is chosen is Case B – IV (Fig. 17). This configuration is for y_{TC} = -215 mm. If compared to Case B – III (Fig. 16), it is possible to observe the conical vortices still originate from corner D. However, the local effects observed for the lateral wall, BC, and the leeward wall, AB, appear to be significantly mitigated.

Another motivation to study Case B – IV is represented by the distance between the tornado core and the center of gravity of the building,

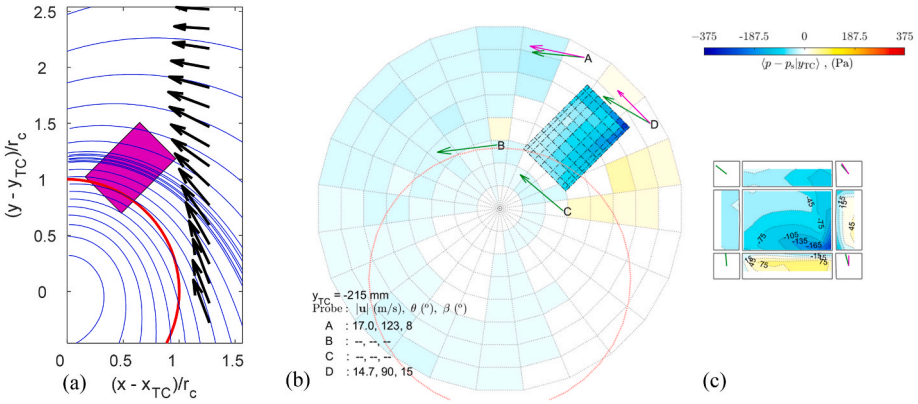

Fig. 17. (a) Tornadic streamlines, (b) mean pressure pattern on the roof and the baseplate, (c) mean pressure pattern on the unfolded building surface for Case B – IV.

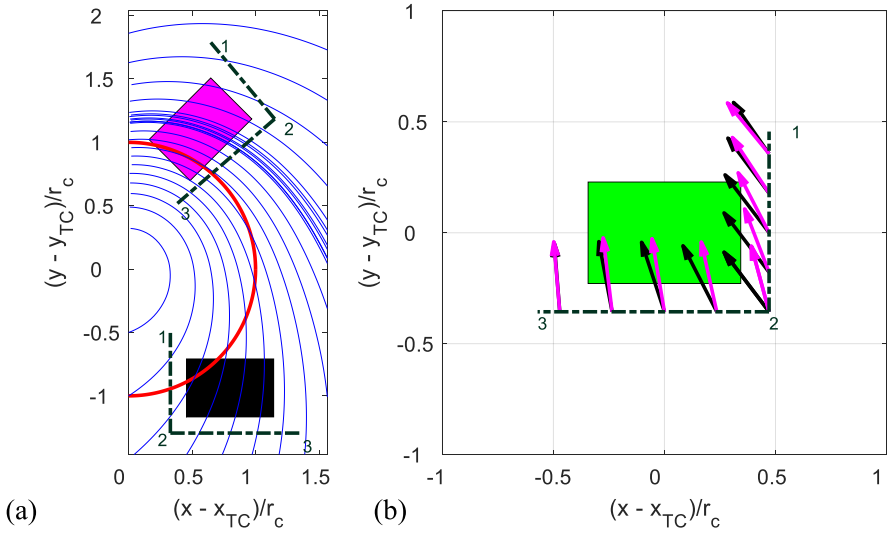

Fig. 18. (a) Identification of the segments $\overline{12}$ and $\overline{23}$ in correspondence of the windward walls for Case A – II and Case B – IV, (b) representation of mean wind velocity vectors along those segments.

1.23 r_0, which is the same as per Case A – II (Fig. 18a). Even beyond that, the wind field in proximity to the windward walls show significant similarities. This may be observed by studying the mean wind velocity vectors that may be estimated from the analytical fit (Section 3) along segments that are parallel to these walls. These are evaluated along the dashed-dotted lines indicated in Fig. 18a. In particular, five points are investigated along the segment $\overline{12}$ to estimate the wind velocity vectors in proximity of the short windward wall of the building (BC for Case A – II and DA for Case B – IV). Analogously, five points are picked along the segment $\overline{23}$ to investigate the wind action acting on the long side CD. Fig. 18b portrays these mean wind velocity vectors for these two cases. To better emphasis the similarity between the two cases, the vectors from Case A – II have been mirrored with respect to the Y-axis of the building (which is colored in green). This plot clarifies that Case A – II is characterized by a lower gradient of the flow direction along the segment $\overline{12}$, while the opposite is found for the segment $\overline{23}$. Nonetheless, the overall variation of the flow direction in the horizontal plane is on the order of 30–35° for both the cases. The magnitudes of the velocity vectors, represented by the length of the arrows, are also comparable between the two cases.

On the other hand, the streamline fields in proximity to the leeward wall of the buildings are significantly different (Fig. 18a). The considerations that have been made concerning the wind field seem to be reflected when examining the mean pressure distributions, which are compared in Fig. 19. For sake of comparison, the distribution of Case A – II has been again mirrored with respect to the Y-axis.

The comparisons between the pressure distributions in Fig. 19 immediately reveal that the conical vortices are generated from the same corner, suggesting the similarity of the incoming wind field. Moreover, the mean overall uplift in the two cases is indeed comparable, being measured in 3.57 N (model scale) for Case A – II and in 3.61 N for Case B – IV. Nonetheless, significant distinctions in the patterns on the roof are unveiled. In fact, albeit the conical vortices are generated from the same corner, the suction generated towards the lateral wall, BC, in Case B – IV seems to be mitigated compared to what is observed in Case A – II towards the corresponding wall, DA. In effect, Case B – IV exhibits the whole edge BC of the roof to be less highly loaded. Moreover, the leeward wall AB presents an increase of the pressure when moving from A to B, not exhibiting any localized suction as in Case A – II. These facts may reflect the presence of a vorticity pattern on the roof in Case B – IV that is different than what discussed when commenting Fig. 12b for Case A – II.

A discussion about the possible causes behind such differences is provided in the following Section.

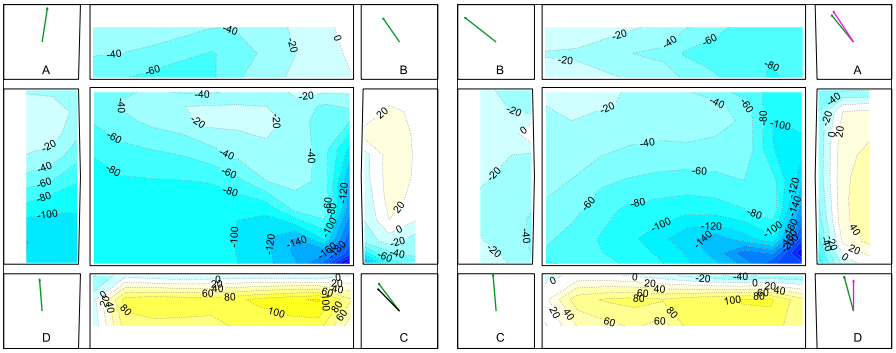

Fig. 19. Mean pressure patterns estimated from Case A – II (mirrored with respect to the Y-axis) and Case B – IV.

5. Discussion

This Section aims to point out the role played by the streamline curvature on the results for cases characterized by similar upstream wind directions. In particular, vorticity patterns are inferred from the mean aerodynamic pressure distributions and discussed. The first couple of cases analyzed derive from Section 4.3 and concern Case A – II and Case B – IV (Fig. 19). As mentioned in Section 4.3, the mechanism associated with the propagation of the vorticity from the originating corner to the peripheral areas of the building seems to be different. In particular, Case A – II (Fig. 19a) shows an increase of the suction in the edges of the roof if compared with Case B –IV. On the other hand, the load seems more comparable, if not reduced, for the intermediate regions between the origin of the conical vortices and the edges of the roof. An increase of the amplification of the vorticity on a wider area for Case A – II may perhaps be induced by the reduction of the component of the velocity vector parallel to the long wall, CD. This may cause a reduction of the vortex-stretching mechanism with respect to ABL winds; hence, the effect of the bubble separation occurring along the edge may become more significant, able to generate an amplification of the vorticity on an area of the roof that is larger than Case B – IV and than ABL winds. Sketches of the vorticity patterns around the building are given in Fig. 20a and b for Case A – II and Case B – IV, respectively. The vorticity amplification occurring on the roof also appears to affect the pattern of the leeward face, AB, with the potential presence of a vortex detached from the corresponding edge of the roof (Fig. 20a). This may explain the strong increase of suction in the inner region of the wall (not observed in Case B – IV), which seems to be detected by pressure taps on the floor as well. Following the same reasoning now for the short side wall (segment $\overline{12}$, Fig. 18b), Case B – IV is characterized by a more significant reduction in the vortex-stretching phenomenon; in effect, also in this case there is a peripheral region (towards the corner A) characterized by an amplification of the vorticity which is broader than what observed for Case A – II along the corresponding wall, BC, associated with a more uniform flow direction. Another comment that may be made concerns the aerodynamic pressure pattern that is found on the lateral wall, DA for Case A – II (Fig. 19a) and BC for Case B – IV (Fig. 19b). The flow separation that is found for Case A – II seems to be much more pronounced, in spite of a similar flow curvature on the associated south-west corner. This different pattern may perhaps be ascribed to the effect of the vertical wind field, which may become of significance in the results from the Case B – IV. In fact, the wall BC is the region that is closest to the tornado core, and the propagation of vorticity on the roof may be awakened by that (Fig. 20b). This may also have implications on the pressure patterns that are found in proximity of the corner B of Case A – II.

The considerations that have just been made seem also to be applicable to explain other different pressure distributions that were observed in Section 4. For instance, this is the case of Case B – I and Case B – II (Section 4.1), whose patterns were found to be different, despite a similar upstream wind field. As illustrated in the sketch in Fig. 21a, the streamline curvature may mitigate the vortex-stretching mechanism occurring along the side CD for Case B – I, and this may generate an amplification of the vorticity affecting the edge of the roof AD, leading to a pattern that appears to be induced by an oblique wind. When the streamline curvature is reduced (Case B – II, Fig. 21b), the conical vortices are no longer present and the distribution becomes more symmetric.

6. Conclusions

In this paper, the role played by the streamline curvature induced by tornado-like flows on the aerodynamics of a low-rise structure is analyzed. Investigations have been conducted through the analyses of conditionally-averaged aerodynamic pressure fields detected by pressure taps installed on the building and on the ground plane. The local wind field has been estimated through the installation of four Cobra probes placed in proximity of the building corners, which allowed the definition of the streamline field of the tornado-like vortex. The building was tested for two different orientations with respect to the tornado translation path, labelled as Cases A and B. Different locations have been selected from Case A and Case B and these have been classified according to the upstream wind direction or according to the distance between the tornado core and the building. Analogies in terms of pressure fields have been found between cases affected by similar streamline fields, suggesting the role played by the streamline curvature as a controlling parameter for the building aerodynamics. On the other hand, these patterns seem to be sensitive to variations of the streamlines field in regions different than the upstream one, in particular in regions affected by the wake. Furthermore, comparisons with those induced by straight-line ABL winds highlights the presence of differences, implying the existence of a different mechanism producing the vortical patterns around the building. This seems to be reflected also by an increase of the aerodynamic loading on walls, specifically on the lateral and leeward sides.

These facts highlight the importance of the variation of the local wind field around the building in the definition of the aerodynamic pressure patterns affecting the structure. The streamline curvature may

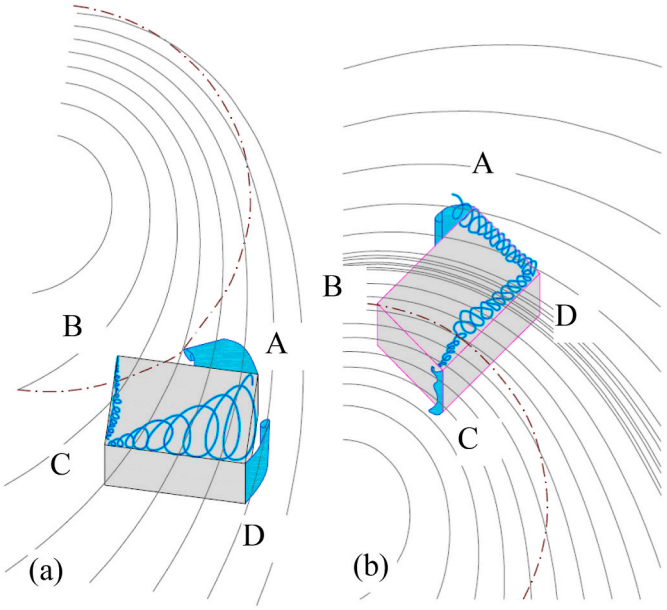

Fig. 20. Sketches of the vorticity patterns generated for (a) Case A – II and (b) Case B – IV.

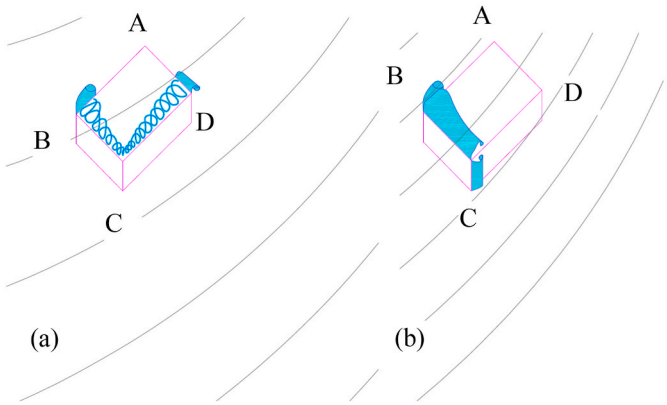

Fig. 21. Sketches of the vorticity patterns generated for (a) Case B – I and (b) Case B – II.

affect the separation bubbles on the wall by shrinking them or affecting their geometry, as well as by modifying the vortical structures on the roof. Further insights may be corroborated by numerical simulations (i.e., CFD) or advanced visualization techniques, such as PIV, which however remain challenging in the framework of tornado simulators. On the other hand, studies conducted in traditional wind tunnels by attempting to replicate a variation in the flow direction may be useful. Reproducing specific aspects of non-synoptic winds in traditional facilities certainly represents an interesting research line for wind engineers, already developed for downbursts (e.g., Solari, 2014; Brusco et al., 2024).

As a future perspective, it would be of great interest to observe how the patterns observed during the presented measurement are sensitive to an increase of the translational velocity of the tornado vortex. In fact, transient aerodynamics constitutes a crucial aspect associated with non-synoptic winds (Brusco et al., 2022). Moreover, a better understanding of the effects of the vertical wind velocity field on the aerodynamics of the building is needed.

CRediT authorship contribution statement

Stefano Brusco: Writing – original draft, Visualization, Validation, Software, Methodology, Investigation, Formal analysis, Data curation, Conceptualization. **Gregory A. Kopp:** Writing – review & editing, Validation, Supervision, Resources, Project administration, Methodology, Investigation, Funding acquisition, Conceptualization.

Declaration of competing interest

The authors declare that they have no known competing financial interests or personal relationships that could have appeared to influence the work reported in this paper.

Data availability

Data will be made available on request.

Acknowledgments

This work was funded by ImpactWX and the University of Western Ontario. The authors are grateful to Drs. Fred Haan, Mark Sterling and Jin Wang for many helpful discussions on this topic. The authors also acknowledge the contribution by Dr. Chieh-Hsun Wu in the organization of the wind tunnel data gathered during the experimental campaign.

References

ASCE 7-22, 2022. Minimum design loads for buildings and other structures. American Society of Civil Engineers.

Baker, C.J., Sterling, M., 2018. A conceptual model for wind and debris impact loading of structures due to tornadoes. J. Wind Eng. Ind. Aerod. 175, 283–291. https://doi.org/10.1016/j.jweia.2017.11.029.

Brusco, S., Buresti, G., Lo, Y.-L., Piccardo, G., 2022. Constant-frequency time cells in the vortex-shedding from a square cylinder in accelerating flows. J. Wind Eng. Ind. Aerod. 230, 105182 https://doi.org/10.1016/j.jweia.2022.105182.

Brusco, S., Bin, H., Lo, Y., Piccardo, G., 2024. Transient aerodynamics of a square cylinder under downburst-like accelerating flows reproduced in a multiple-fan wind tunnel. J. Fluid. Struct. 104038 https://doi.org/10.1016/j.jfluidstructs.2023.104038.

Chen, Q., Tang, Z., Wu, X., Zuo, D., James, J., 2023. Laboratory study of tornado-like loading on a low-rise building model. J. Wind Eng. Ind. Aerod. 238 https://doi.org/10.1016/j.jweia.2018.12.013.

Davenport, A.G., 1961. The application of statistical concepts to the wind loading of structures. Proc. Inst. Civ. Eng. 19 (4), 449–472.

Davies-Jones, R.P., 1986. In: Kessler, E. (Ed.), Tornado Dynamics. Thunderstorms Morphology and Dynamics, 2d ed. University of Oklahoma Press.

Gairola, A., Bitsuamlak, G., 2019. Numerical tornado modeling for common interpretation of experimental simulators. J. Wind Eng. Ind. Aerod. 186, 32–48. https://doi.org/10.1016/j.jweia.2018.12.013.

Gairola, A., Bitsuamlak, G.T., Hangan, H.M., 2023. An investigation of the effect of surface roughness on the mean flow properties of "tornado-like" vortices using large eddy simulations. J. Wind Eng. Ind. Aerod. 234, 105348 https://doi.org/10.1016/j.jweia.2023.105348.

Gairola, A., Bitsuamlak, G.T., Hangan, H.M., 2024. The effect of swirl ratio and surface roughness on the boundary layer of "tornado-like" vortices. J. Wind Eng. Ind. Aerod. 252, 105841. https://doi.org/10.1016/j.jweia.2024.105841.

Groenemejer, P., Kühne, T., 2014. A climatology of tornadoes in Europe: results from the European severe weather database. Mon. Weather Rev. 142, 4775–4790. https://doi.org/10.1175/MWR-D-14-00107.1. American Meteorological Society.

Haan Jr., F.L., Wang, J., Sterling, M., Kopp, G.A., 2024. Experimentally estimating wind load coefficients for tornadoes – an alternative perspective. J. Wind Eng. Ind. Aerod. 251, 105811 https://doi.org/10.1016/j.jweia.2024.105811.

Hu, H., Yang, Z., Sarkar, P., Haan, F., 2011. Characterization of the wind loads and flow fields around a gable-roof building model in tornado-like winds. Exp. Fluid 51, 835–851. https://doi.org/10.1007/s00348-011-1102-6.

Kopp, G.A., Wu, C.H., 2020. A framework to compare wind loads on low-rise buildings in tornadoes and atmospheric boundary layers. J. Wind Eng. Ind. Aerod. 204, 104269 https://doi.org/10.1016/j.jweia.2020.104269.

Kopp, G.A., Surry, D., Mans, C., 2005. Wind effects of parapets on low buildings: Part 1. Basic aerodynamics and local loads. J. Wind Eng. Ind. Aerod. 93, 817–841. https://doi.org/10.1016/j.jweia.2005.08.006.

Lombardo, F.T., 2018. Engineering analysis of a full-scale high-resolution tornado wind speed record. J. Struct. Eng. 144 (2), 04017212 https://doi.org/10.1061/(ASCE)ST.1943-541X.0001942.

Lombardo, F.T., Zaldivar de Alba, A., Chen, G., Rhee, D.M., Nevill, J.B., Wienhoff, Z.B., 2023. An atmospheric vortex and its induced loading on a bluff body. J. Wind Eng. Ind. Aerod. 243, 105605 https://doi.org/10.1016/j.jweia.2023.105605.

Miller, C.S., Kopp, G.A., Sills, D.M., Butt, D.G., 2024. Estimating wind speeds in tornadoes using debris trajectories of large compact objects. Mon. Weather Rev. https://doi.org/10.1175/MWR-D-23-0251.1.

Refan, M., Hangan, H., 2016. Characterization of tornado-like flow fields in a new model scale wind testing chamber. J. Wind Eng. Ind. Aerod. 151, 107–121. https://doi.org/10.1016/j.jweia.2016.02.002.

Refan, M., Hangan, H., 2018. Near surface experimental exploration of tornado vortices. J. Wind Eng. Ind. Aerod. 175, 120–135. https://doi.org/10.1016/j.jweia.2018.01.042.

Romanic, D., Shoji, H., Hangan, H., 2023. Experimental investigation of surface pressures, velocities, and dynamic structural analysis of tornadic winds on a luminary pole. J. Fluid. Struct. 116, 103794. https://doi.org/10.1016/j.jfluidstructs.2022.103794.

Sills, D.M.L., Kopp, G.A., Lesley, El, Jaffe, A.L., Sutherland, L., Miller, C.S., Kunkel, J.M., Hong, E., Stevenson, S.A., Wang, W., 2020. The northern tornadoes project: unvovering Canada's true tornado climatology. B. Am. Metereol. Soc. 101 (12), E2113–E2132. https://doi.org/10.1175/BAMS-D-20-0012.1.

Solari, G., 2014. Emerging issues and new frameworks for wind loading on structures in mixed climates. Wind Struct. 19, 295–320. https://doi.org/10.12989/was.2014.19.3.295.

Stevenson, S.A., Miller, C.S., Sills, D.M.L., Kopp, G.A., Rhee, D.M., Lombardo, F.T., 2023. Assessment of wind speeds along the damage path of the Alonsa, Manitoba EF4 tornado on 3 August 2018. J. Wind Eng. Ind. Aerod. 238, 105422 https://doi.org/10.1016/j.jweia.2023.105422.

Wang, J., Cao, S., Pang, W., Cao, J., 2017. Experimental Study on Effects of Ground Roughness on Flow Characteristics of Tornado-like Vortices, Boundary-Layer Meterol, 162, pp. 319–339. https://doi.org/10.1016/j.jweia.2020.104269.

Wang, M., Cao, S., Cao, J., 2022. Numerical study on applicability of various swirl ratio definitions to characterization of tornado-like vortex flow field. J. Wind Eng. Ind. Aerod. 220, 104841 https://doi.org/10.1016/j.jweia.2021.104841.

Wu, C.-H., Kopp, G.A., 2016. Estimation of wind-induced pressures on a low-rise building using quasi-steady theory. Frontiers Built Env 2, 5. https://doi.org/10.3389/fbuil.2016.00005.

Wu, C.-H., Kopp, G.A., 2018. A quasi-steady model to account for the effects of upstream turbulence characteristics on pressure fluctuations on a low-rise building. J. Wind Eng. Ind. Aerod. 179, 338–357. https://doi.org/10.1016/j.jweia.2018.06.014.

Yang, Z., Sarkar, P., Hu, H., 2011. An experimental study of a high-rise building model in tornado-like winds. J. Fluid. Struct. 27 (4), 471–486. https://doi.org/10.1016/j.jfluidstructs.2011.02.011.

Yang, Q., Gao, R., Bai, F., Li, T., Tamura, Y., 2018. Damage to buildings and structures due to recent devastating wind hazards in East Asia. Nat. Hazards: Journal of the International Society for the Prevention and Mitigation of Natural Hazards 92 (3), 1321–1353. https://doi.org/10.1007/s11069-018-3253-8.

Zhang, D., Liu, Z., Jiang, X., Jiang, W., Gao, H., Li, C., Xiao, Y., Hu, G., 2023. Numerical study of flow characteristics of tornado-like vortices considering both swirl ratio and aspect ratio. J. Wind Eng. Ind. Aerod. 240, 105468 https://doi.org/10.1016/j.jweia.2023.105468.

Zuo, D., Tang, Z., Zhang, H., James, D., Eguchi, Y., 2021. Narrowband components in two-celled tornado-like vortices generated in a Ward-type simulator. J. Wind Eng. Ind. Aerod. 218, 104767 https://doi.org/10.1016/j.jweia.2021.104767.